Transactions on Computer Science and Intelligent Systems Research
ISSN: 2960-1800, eISSN: 2960-2238 | Volume 11
TPCEE 2025

Fringe Projection-Based 3D Surface Measurement System

Rujia Yang
Tsinglan School, Guangdong, China
2469857616@qq.com

Abstract. Three-dimensional measurement technology is widely used in scientific research and industrial fields. With the advancement of the era, traditional contact measurement methods, due to their low imaging accuracy, slow measurement speed, and limited applicability—being unable to measure elastic or deformable objects—are gradually failing to meet the demands of modern industrial development. As a novel 3D imaging approach, non-contact optical three-dimensional measurement technology offers the advantages of high precision, large field of view, and non-destructive inspection without requiring physical contact with the object. This project designs and implements a high-speed 3D surface measurement system based on fringe projection, utilizing non-contact optical three-dimensional measurement technology. By combining spatial and frequency domain analysis, the study investigates the reconstruction effects of the four-step phase-shifting method and Fourier transform profilometry on the 3D surface morphology of objects. Based on this, an independent system algorithm is developed, ultimately achieving an integrated system design. The proposed system not only meets the practical application requirements of intelligent manufacturing and cultural relic preservation but also serves as an optical experimental teaching platform, helping students better understand fringe projection, phase retrieval, and their real-world applications.

Keywords: Fringe projection; Three-dimensional imaging; Structured light measurement; Interferometric recording.

1. Introduction

With the rise of the fourth industrial revolution, global manufacturing has undergone profound transformations, gradually transitioning toward intelligent manufacturing supported by new-generation information technologies. Policies such as *Made in China 2025* explicitly state the need to "use the deep integration of informatization and industrialization to lead and drive the development of the entire manufacturing industry," providing strategic requirements and guidance for the development of China's traditional manufacturing sector. This aims to achieve technological innovation and optimize the quality and structure of products, which necessitates the support of high-precision machining equipment and inspection technologies [1]. Fringe projection-based 3D imaging technology, due to its significant advantages such as non-contact operation, high precision, high speed, large field of view, and ease of use, has been widely applied in intelligent manufacturing inspection, product quality assessment, cultural heritage digitization, reverse engineering, and material performance testing, among other fields. For example, in high-precision optical systems, the surface and subsurface quality of optical components directly affect the resolution and energy absorption of the entire system. However, mechanical processing of optical components inevitably causes some degree of mechanical damage to optical glass, and the resulting surface and subsurface defects can severely impact the optical performance of the system. Therefore, rapid and precise detection and evaluation of the surface and subsurface structures of precision optical components play a crucial role in the development of optical systems [2]. In the maintenance of precision equipment components, such as those in aircraft and rockets, traditional inspection methods—such as dial indicators (which cannot identify micro-defects due to the limitations of the probe tip) and laser-based methods (which cannot guarantee that the measurement result corresponds to the maximum defect depth)—struggle to achieve defect detection on complex curved surfaces. Additionally, the presence of contact force during measurement may introduce new damage to the inspected surface, and the single-point

Content from this work may be used under the terms of CC BY-NC 4.0 licence (https://creativecommons.org/licenses/by-nc/4.0/).
Published by Warwick Evans Publishing.

measurement approach significantly prolongs inspection time [3]. Furthermore, assessing the corrosion resistance, thermal expansion coefficient, and stress-strain behavior of new materials under extreme environments is critical for evaluating their performance. In this context, the development of faster, higher-precision, non-contact, and large-field-of-view 3D imaging instruments has become increasingly important.

Furthermore, as a crucial component of university physics laboratory education, optical experiments serve as powerful tools to cultivate students' disciplinary interest and experimental literacy while deepening their understanding of theoretical knowledge. However, most existing teaching instruments primarily focus on demonstrating classical theoretical knowledge and optical phenomena, with relatively low levels of informatization, making it difficult for students to connect theoretical concepts with practical applications. Additionally, current university laboratory education lacks experimental apparatus that effectively combines spatial and frequency domain analyses, and the teaching process often fails to establish clear connections between optical phenomena and their corresponding spatial/frequency domain transformations. Therefore, accelerating the innovation and improvement of university laboratory equipment, expanding students' exposure to practical applications of optical theory, and strengthening their comprehension of the relationships between experimental phenomena and corresponding parameter variations remain critical challenges to be addressed in contemporary higher education.

In summary, fringe projection-based 3D imaging technology plays a significant role in both practical technical applications and higher education. It not only enables non-destructive testing of precision machined components but also effectively combines the knowledge of wedge interference fringe distortion with practical applications. By integrating spatial and frequency domain analyses, this technology helps students visualize optical theoretical knowledge and its practical implementations, thereby deepening their understanding of spatial-frequency domain relationships. This dual functionality makes it an invaluable tool for both industrial applications and educational advancement.

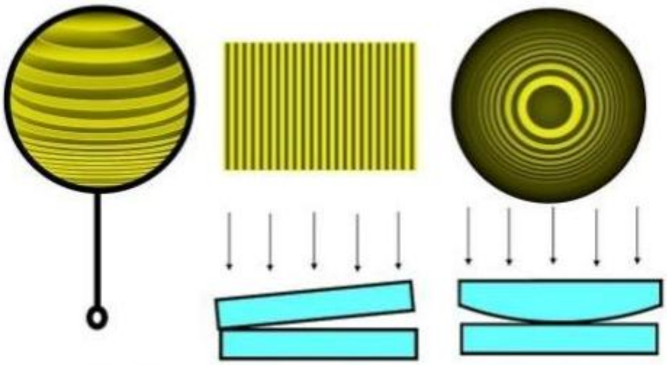

Figure 1. Experimental teaching

Figure 2. Component inspection

2. Basic Principles

2.1. Principle of Fringe Projection Structured Light Measurement

The principle of projection-based structured light measurement is illustrated in Fig. 3. The system employs a DMD (Digital Micromirror Device) to display encoded sinusoidal fringe patterns, which are projected onto the target object. A CMOS camera then captures the deformed fringe patterns modulated by the object's surface. The fringe deformation reflects the height variations of the object's surface - by demodulating the phase shift of the deformed fringes, the corresponding height information can be determined.

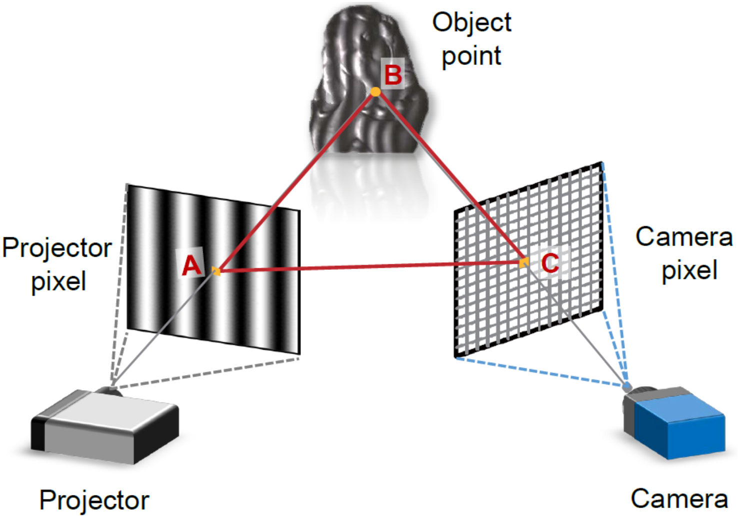

Figure 3. Schematic diagram of structured light measurement system

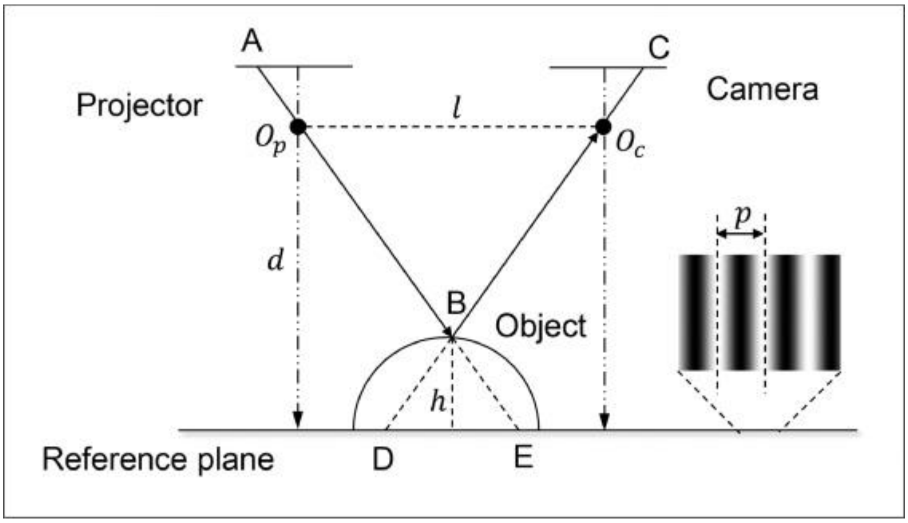

Figure 4. Parallel-axis system schematic

The DMD projects the encoded sinusoidal fringe patterns onto the reference plane, and the fringe patterns received by the CMOS camera can be expressed as:

$$I_0(x,y) = A(x,y) + B(x,y)\cos\left(\frac{2\pi x}{p} + \varphi(x,y)\right) \tag{1}$$

Where: (x,y) are pixel coordinates, $I_0(x,y)$ represents the reference plane intensity distribution, $A(x,y)$ is background intensity distribution, $B(x,y)$ denotes modulation intensity distribution, p is the structured light fringe period, and $\varphi(x,y)$ is the phase modulated by the reference plane.

The DMD projects the encoded sinusoidal fringe patterns onto the object surface, and the fringe patterns received by the CMOS camera can be expressed as:

$$I(x,y) = A(x,y) + B(x,y)\cos\left(\frac{2\pi x}{p} + \varphi(x,y) + \phi(x,y)\right) \tag{2}$$

Where: $\mathrm{I}(\mathrm{x},\mathrm{y})$ represents the intensity distribution after the object is introduced, and $\phi(\mathrm{x},\mathrm{y})$ denotes the phase modulated by the object, which is determined by the relative height of the object at (x,y). Therefore, recovering $\phi(\mathrm{x},\mathrm{y})$ allows the acquisition of the object's three-dimensional topography.

2.2. Phase Calculation

2.2.1. Fourier Transform Profilometry (FTP).

FTP can achieve phase recovery with a single frame image. Its core process is as follows: First, perform Fourier transform on the deformed fringe pattern containing object height information to obtain the frequency domain distribution; then design a digital filter to extract one of the first-order spectral components while suppressing the fundamental frequency and noise; next, perform inverse Fourier transform on the selected spectrum, and calculate the arctangent based on the real and imaginary parts of the resulting complex signal to demodulate the continuous wrapped phase. This technology requires only a single image, offering extremely high processing efficiency, and is widely used in dynamic profile measurement, high-speed process monitoring, and other scenarios. In Matlab simulations, the first step is to generate ideal sinusoidal fringes of a certain frequency. After projecting these fringes onto the surface of the object to be measured, they become deformed due to surface height modulation, and the grayscale of the final fringe image captured by the camera can be expressed as:

$$I_0(x,y) = A(x,y) + B(x,y)\, cos\big(2\pi f_0 x + \phi(x,y)\big) \tag{3}$$

Where: (x,y) are pixel coordinates; $A(x,y)$ represents background intensity distribution; $B(x,y)$ denotes modulation intensity distribution; f_0 is the structured light fringe frequency; $\phi(x,y)$ is the phase modulated by the object surface.

This equation is equivalent to:

$$I_0(x,y) = A(x,y) + C(x,y)e^{i2\pi f_0 x} + C^*(x,y)e^{-i2\pi f_0 x} \tag{4}$$

Where:

$$C(x,y) = \frac{1}{2}B(x,y) \tag{5}$$

$$C^*(x,y) = \frac{1}{2}B(x,y)e^{-i\phi(x,y)} \tag{6}$$

Performing a two-dimensional Fourier transform on the above equation yields:

$$G(u,v) = a(u,v) + c(u-f_0,y) + c^*(u+f_0,v) \tag{7}$$

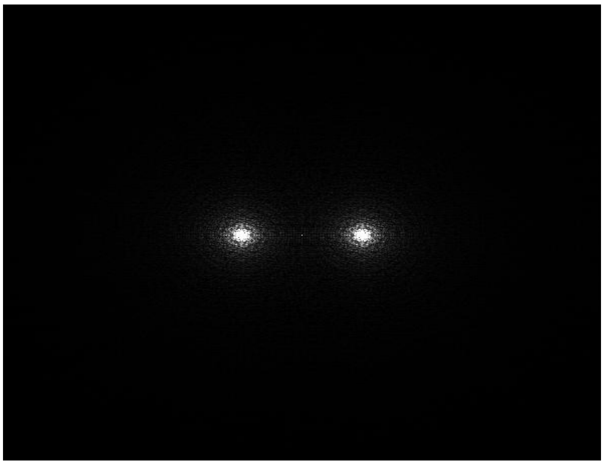

Figure 5. Fourier transform frequency domain

As shown in Fig. 5, the fundamental frequency is located at the center of the spectrum, while the symmetric first-order spectra on both sides contain phase information. After filtering out the fundamental frequency, an inverse Fourier transform is performed on the retained first-order spectrum to obtain the complex signal. The phase is then calculated using the following equation:

$$\phi(x, y) = \tan^{-1}\left(\frac{Im(g(x,y))}{Re(g(x,y))}\right) \tag{8}$$

Where: Im denotes taking the imaginary part, and Re denotes taking the real part. Since the arctangent function is used here, the obtained phase is truncated and requires phase unwrapping.

Fourier Transform Profilometry uses only one fringe image for calculation, offering fast processing speed and good performance when the object surface is smooth with low noise. However, during filtering, it requires that the zero-order spectrum and first-order spectrum do not overlap, resulting in relatively lower accuracy compared to phase-shifting methods.

2.2.2. Phase-Shifting Method.

The phase-shifting method reconstructs the phase distribution by projecting multiple fringe patterns with fixed phase shifts onto the object under test. Since it requires capturing a larger number of images, its data acquisition and processing speed are typically slower than FTP, which only needs a single image, thus limiting its application in dynamic measurement scenarios. However, the phase-shifting method has unique advantages: it does not require frequency-domain filtering during phase extraction, avoiding errors introduced by filter design, and all calculations are performed pixel-by-pixel in the spatial domain, making its principle intuitive and its computation stable.

The intensity distribution of the fringe patterns encoded by the standard N-step phase-shifting method is given by:

$$I_i(x, y) = A(x, y) + B(x, y)\cos(\phi(x, y) + \delta_i) \tag{9}$$

Where: $\mathrm{I_i(x, y)}$ represents the intensity distribution of the i-th fringe pattern, $\phi(\mathrm{x, y})$ denotes the fringe phase distribution, δ_i indicates the phase shift amount taken as $\delta_\mathrm{i} = \frac{(\mathrm{i}-1)2\pi}{\mathrm{N}}$, N is the total number of phase-shifting steps. Since the equation contains three unknowns, $\mathrm{N} \geq 3$ must be satisfied to solve for $\phi(\mathrm{x, y})$.

$$\hat{\phi}(x, y) = -\tan^{-1}\left(\frac{\sum_{i=1}^{N} I_i \sin\frac{2(i-1)\pi}{N}}{\sum_{i=1}^{N} I_i \cos\frac{2(i-1)\pi}{N}}\right) \tag{10}$$

Where: tan^{-1} represents the four-quadrant arctangent function, thus $-\pi < \hat{\phi}(x,y) \leq \pi$.

This experiment adopts the four-step phase-shifting method with $N = 4$, fringe frequency $f = 64$, and phase shifts of $0, \pi/2,\ \pi, 3\pi/2$ sequentially. The intensity distributions of the four fringe patterns are as follows:

$$I_1(x,y) = A(x,y) + B(x,y)\cos\big(\phi(x,y)\big) \tag{11}$$

$$I_2(x,y) = A(x,y) - B(x,y)\sin\big(\phi(x,y)\big) \tag{12}$$

$$I_3(x,y) = A(x,y) - B(x,y)\cos\big(\phi(x,y)\big) \tag{13}$$

$$I_4(x,y) = A(x,y) + B(x,y)\sin\big(\phi(x,y)\big) \tag{14}$$

The four fringe patterns generated in Matlab according to the above equation are shown in Fig. 6:

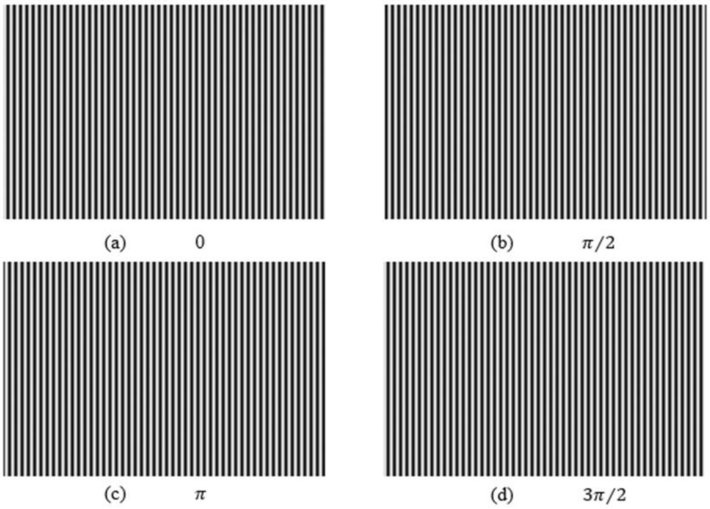

Figure 6. Four-step phase-shifting fringe patterns

Obtain the truncated phase distribution:

2.3. Phase Unwrapping - Multi-Frequency Heterodyne Method

Phase wrapping occurs because the arctangent function can only map phase values to the range [-π, π], causing the truncated integer multiples of 2π in the true phase to be unrecoverable, resulting in a sawtooth-like discontinuous distribution. To calculate the three-dimensional information of the measured object from the phase distribution, the phase distribution of the object must possess uniqueness.

2.3.1. Principle.

The phase-shifting method employs an arctangent operation, resulting in a discontinuous phase with 2π jumps. The purpose of phase unwrapping is to determine the integer fringe order $k(x,y)$ and eliminate these 2π discontinuities, as shown in Fig. 7:

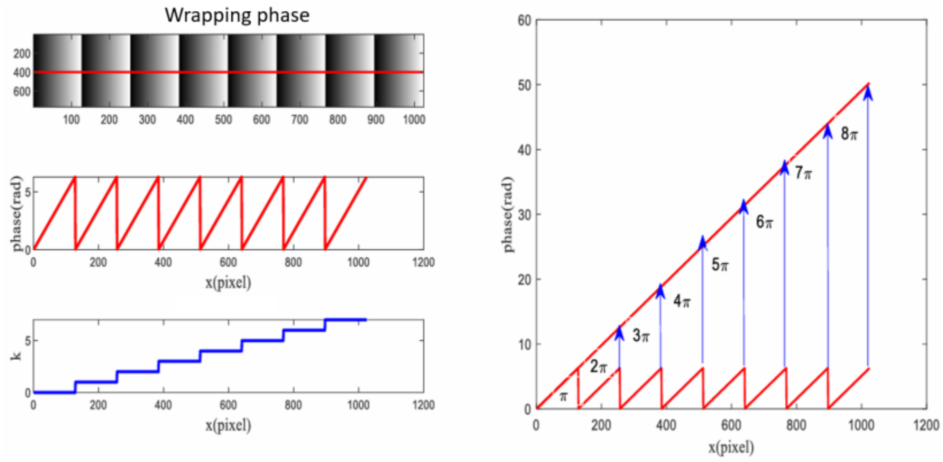

Figure 7. Phase unwrapping principle schematic diagram

The unwrapped phase can be calculated using the following equation:

$$\phi(x,y) = \hat{\phi}(x,y) + 2k(x,y)\pi \tag{15}$$

Where: $k(x,y)$ is the fringe order distribution.

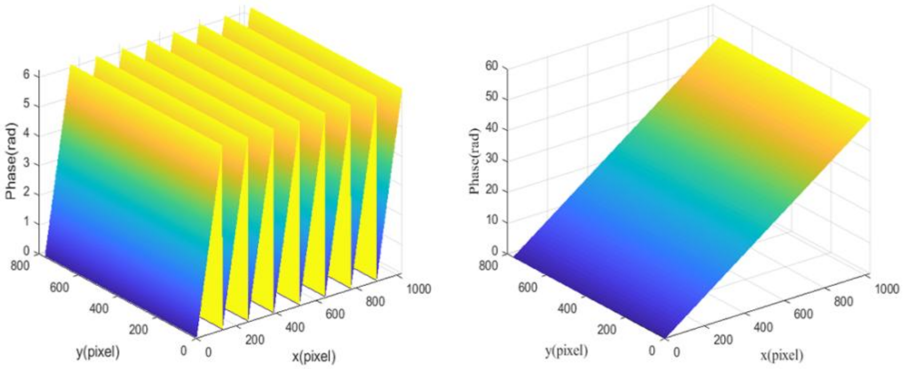

Figure 8. Wrapped phase (left) and unwrapped phase (right) in 2D

2.3.2. Multi-Frequency Heterodyne Method.

Based on the empirical formula above, we selected fringe frequencies of $f_1 = 73$, $f_2 = 64$, $f_3 = 56$ respectively. After obtaining the corresponding phases $\hat{\phi}_1$, $\hat{\phi}_2$, $\hat{\phi}_3$ for each frequency (*i*=1, 2, 3) using the four-step phase-shifting method, we performed pairwise heterodyne processing to derive:

$$\hat{\phi}_{12} = \begin{cases} \hat{\phi}_1 - \hat{\phi}_2 \\ \hat{\phi}_2 - \hat{\phi}_1 + 2\pi \end{cases} \tag{16}$$

$$\hat{\phi}_{23} = \begin{cases} \hat{\phi}_2 - \hat{\phi}_3 \\ \hat{\phi}_3 - \hat{\phi}_2 + 2\pi \end{cases} \tag{17}$$

$$\hat{\phi}_{12} = \begin{cases} \hat{\phi}_{12} - \hat{\phi}_{23} \\ \hat{\phi}_{23} - \hat{\phi}_{12} + 2\pi \end{cases} \tag{18}$$

Where: $\hat{\phi}_{12}$, $\hat{\phi}_{23}$, $\hat{\phi}_{123}$ represent the heterodyned phase.

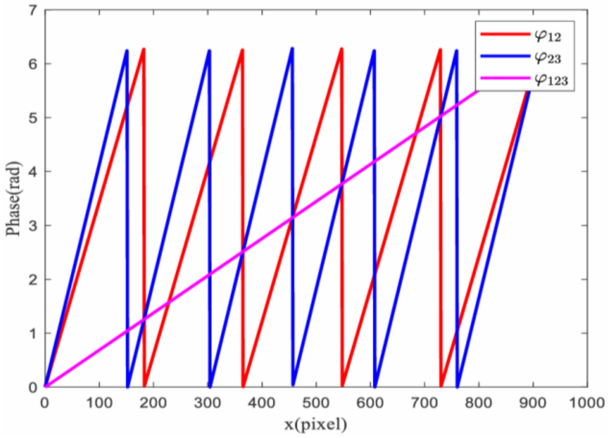

Figure 9. Heterodyned phase pattern

Fringe frequency after heterodyning:

$$f_{12} = f_1 - f_2 \tag{19}$$

$$f_{23} = f_2 - f_3 \tag{20}$$

$$f_{123} = f_{12} - f_{23} \tag{21}$$

To reconstruct using the high-frequency phase, we need to obtain the unwrapped phase of $\hat{\phi}_1$. Progressive phase unwrapping can reduce the impact of noise introduced by heterodyning on the fringe order calculation. The final continuous phase at the highest frequency is obtained as:

$$\mathrm{k}_{12} = \mathrm{round}\left(\frac{\mathrm{f}_{12}/\mathrm{f}_{23} \times \hat{\phi}_{123} - \hat{\phi}_{12}}{2\pi}\right) \tag{22}$$

$$\phi_{12} = \hat{\phi}_{12} + 2\mathrm{k}_{12}\pi \tag{23}$$

$$\mathrm{k}_1 = \mathrm{round}\left(\frac{\mathrm{f}_1/\mathrm{f}_{12} \times \hat{\phi}_{12} - \hat{\phi}_1}{2\pi}\right) \tag{24}$$

$$\phi_1 = \hat{\phi}_1 + 2\mathrm{k}_1\pi \tag{25}$$

Where: ϕ_{12} and ϕ_1 are the unwrapped phases of $\hat{\phi}_{12}$ and $\hat{\phi}_1$, respectively [4].

The detailed phase unwrapping process is illustrated in Fig. 10:

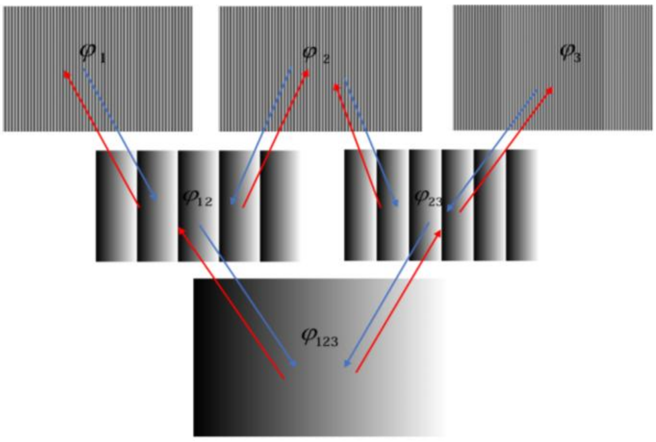

Figure 10. Schematic diagram of three-frequency heterodyne phase unwrapping

3. Experimental System Design and Setup

3.1. System Hardware

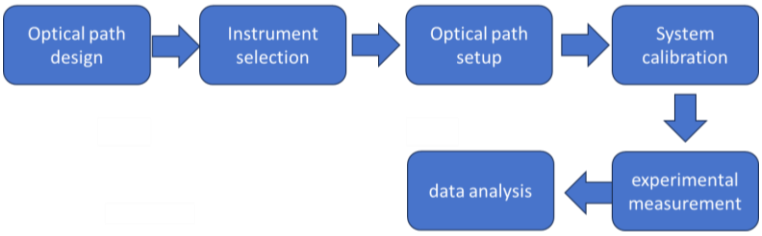

Figure 11. Overall design approach

3.1.1. Experimental Optical Path Design.

To achieve large field-of-view, high-speed, and high-precision measurements in the fringe projection imaging system, we designed the experimental optical path based on the active area-structured light method. As shown in Fig. 12, the measurement system is primarily divided into a fringe projection unit, an image acquisition unit, and a fringe analysis unit. The grating pattern generated by the fringe projection unit is projected onto the reference plane of the object under test through a projection lens, causing corresponding degrees of fringe distortion due to variations in the object's surface gradient. The image acquisition unit, positioned at another angle, captures the distorted interference fringes containing the object's phase information via spatial reflection. These fringes are then uploaded to a computer for algorithmic processing, ultimately reconstructing the three-dimensional morphology of the object.

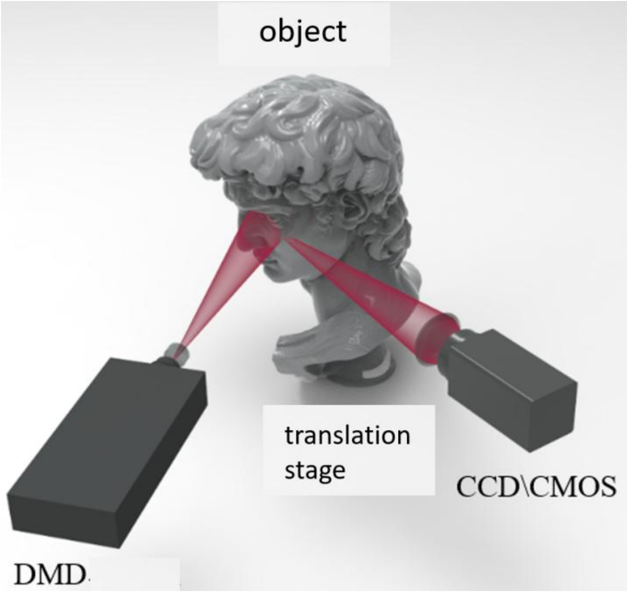

Figure 12. Theoretical Optical Path of Fringe Projection System

3.1.2. Fringe Projection Method Selection.

In active area-structured light measurement systems, the resolution of encoded fringe patterns directly determines the accuracy of measurement data. Thus, acquiring high-density, high-resolution fringe images becomes a primary challenge. Currently, common fringe projection methods include digital projectors (DMD), grating-based fringe projection, and fiber-optic interferometric fringe projection.

Grating-based fringe projection typically employs a fixed grating to generate predefined fringe patterns, which are static rather than dynamically generated. While this method offers advantages such as simplicity and strong stability, its pre-set patterns cannot be easily modified or adaptively adjusted for different objects or environments, resulting in poor flexibility. Additionally, the limited resolution of physical gratings constrains measurement accuracy.

Fiber-optic interferometric fringe projection creates fringe patterns through laser interference on the object surface. Leveraging the interference effect, it can produce extremely fine fringe patterns by adjusting the laser wavelength and interference angle. This approach offers high precision, minimal optical interference, and the ability to measure microstructures. However, its complex setup demands high-end laser interference equipment and exceptional optical stability, making it difficult to implement and costly. Moreover, the small fringe spacing inherent to interference patterns limits the measurement range, rendering it unsuitable for large-field-of-view applications.

In contrast, DLP (Digital Light Processing) technology utilizes a digital micromirror array to generate and modulate fringe patterns, which are projected onto the object surface via a light source. The projected patterns can be dynamically controlled and adjusted in real-time via computer software. This method achieves high resolution, fast response, and exceptional flexibility and adaptability in fringe generation. It is particularly suitable for large-scale object measurements. Therefore, we selected DLP as the fringe projection unit for our system [6].

3.1.3. Theoretical Accuracy of the System.

The resolution of a DMD (Digital Micromirror Device) can be expressed as:

$$R_w \times R_h \tag{26}$$

The size of the measured object can be expressed as:

$$W \times H \tag{27}$$

We can calculate the number of pixels per millimeter projected onto the object surface, known as pixel density. The pixel density in the width direction is expressed as:

$$P_W = \frac{R_w}{W} \tag{28}$$

The pixel density in the height direction is given by:

$$P_h = \frac{R_h}{H} \tag{29}$$

The theoretical measurement accuracy is inversely related to pixel density, and the actual physical size covered by each pixel is given by:

$$ppi_x = \frac{1\,mm}{P_w} \tag{30}$$

$$ppi_y = \frac{1\,mm}{P_h} \tag{31}$$

As demonstrated by the above equations, a higher DMD resolution directly increases the pixel density per unit area, thereby reducing the measurement accuracy value and ultimately enhancing the system's limiting resolution.

3.1.4. Component Selection for the System.

(1) Stripe Projection Unit: To meet the system's requirements for high precision and high-speed performance, the projection unit must employ a model with high resolution, high frame rate, and a long working distance. This system adopts the DLP4500 optical engine as the projection module, which supports both video and sequence projection modes. In sequence mode, users can project image

sequences frame by frame and flexibly configure parameters such as the exposure time and inter-frame interval for each pattern. In this mode, the device can achieve a projection rate of up to 120 frames per second for 8-bit grayscale images.

(2) Image Acquisition Unit: When interference fringes are projected onto the surface of the object under test, a photoelectric imaging device is required to record the distorted fringes in real time. We selected the Daheng Imaging HD-G508M-U3 industrial-grade digital camera, which has a resolution of 2448×2048 pixels, a maximum frame rate of 70 FPS, and a pixel size of 3.45 µm. Its photosensitive area measures 8.446×7.066 mm, enabling real-time dynamic capture. The camera offers advantages such as a large target surface, high resolution, low noise, ease of use, and reliable stability.

(3) Lens: The selection of lenses must consider factors such as lens mount, focal length, and target size. The projection lens uses the Computar MPW2 series with a focal length of 25 mm, a sensor size of 2/3", and an F-number of 1.8. The imaging lens employs the Computar MP2 series, featuring a 16 mm focal length and an F-number of 1.4.

3.1.5. Instrument Setup and Parameter Calibration.

Before the actual optical setup, it is necessary to pre-encode the grating patterns required for the experiment using a computer. When the grating patterns are sinusoidal fringes, the technique is referred to as Fringe Projection Profilometry (FPP). The use of sinusoidal fringes enhances the resolution and accuracy of the 3D data obtained through fringe projection technology.

Therefore, we employ Matlab to generate fringe patterns with a /2 phase-shift period. The resulting interference fringes are shown in Fig. 6. As illustrated in Fig. 13, prior to assembling the system, we first set up the optical path on the experimental platform. Through system calibration experiments, we determine the instrument's position and orientation, followed by adjustments to the optical parameters.

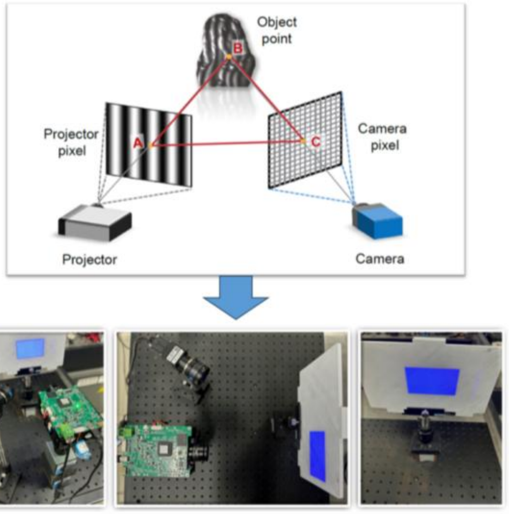

Figure 13. Experimental Optical Path Setup

After completing the experimental optical path setup, we designed the structural configuration of the fringe projection system using 3D modeling software SolidWorks 2022. Through structural analysis of the instrument, we identified that the extrinsic parameters of the DMD and CMOS would significantly affect measurement accuracy. To minimize measurement errors, we rigidly fixed both the DMD and CMOS modules to achieve an integrated mechanical structure, thereby preventing alterations in their extrinsic parameters during system operation or transportation that could compromise imaging quality.

During experiments, we observed that the fringe patterns captured by the CMOS contained shadow artifacts due to limited viewing angles, which degraded imaging performance. Furthermore, the fixed pose of the CMOS prevented comprehensive 3D reconstruction of the measured object's full topography. To address these issues, we incorporated a horizontal rotary stage beneath the test object. This rotational mechanism enables multi-angle measurements by rotating the target object, thereby simplifying system architecture while achieving complete 3D surface reconstruction.

Through iterative optical path and structural design of the fringe projection system, we ultimately developed the following system model: The CMOS was calibrated using Zhang's checkerboard calibration method to obtain its intrinsic parameters. The extrinsic parameters were then derived by combining these intrinsic parameters with the CMOS imaging model, enabling precise determination of the measured object's position. By fixing the relative positions and angles between the DMD, CMOS, and the measured object, we ensured that the interference fringes propagated without deviation, allowing the fringe patterns to project uniformly and perpendicularly onto the reference plane of the measured object. The horizontal rotary stage allowed for adjustable measurement angles, effectively reducing shadow effects caused by surface undulations of the measured object. During experiments, we observed flickering in the images captured by the CMOS, which distorted the interference fringes projected onto the object's surface. Further experimentation revealed that reducing the aperture range of the CMOS imaging lens not only eliminated fringe distortion caused by flickering but also effectively increased the depth of field, resulting in clearer measurement images. Additionally, using a projection lens with a longer focal length further enhanced the depth of field and expanded the adjustable distance for the object. Based on the experimental model design and testing, we completed the assembly and machining of the instrument, with the final prototype shown in Fig. 14.

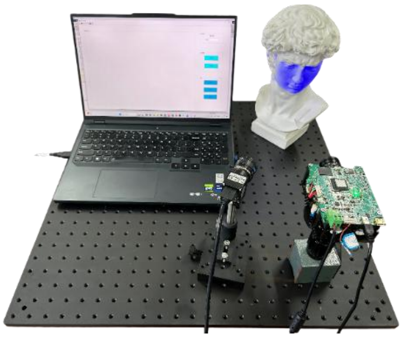

Figure 14. Instrument Prototype

3.2. System Software

3.2.1. Simulation.

To identify optimal experimental parameters and improve efficiency prior to actual testing, we conducted a series of theoretical simulations using MATLAB, shown in Fig. 15.

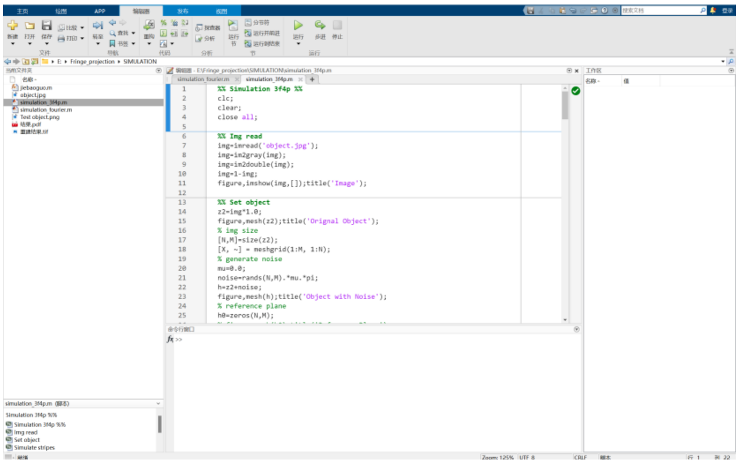

```
%% Simulation 3f4p %%
clc;
clear;
close all;

%% Img read
img=imread('object.jpg');
img=im2gray(img);
img=im2double(img);
img=1-img;
figure,imshow(img,[]);title('Image');

%% Set object
z2=img*1.0;
figure,mesh(z2);title('Orignal Object');
% img size
[N,M]=size(z2);
[X, ~] = meshgrid(1:M, 1:N);
% generate noise
mu=0.0;
noise=rands(N,M).*mu.*pi;
h=z2+noise;
figure,mesh(h);title('Object with Noise');
% reference plane
h0=zeros(N,M);
```

Figure 15. Simulation Platform Schematic Diagram

We conducted separate simulation analyses of the spatial-domain-based Fourier Transform Profilometry and the frequency-domain-based Three-Frequency Four-Phase method, with the results shown in Fig. 16.

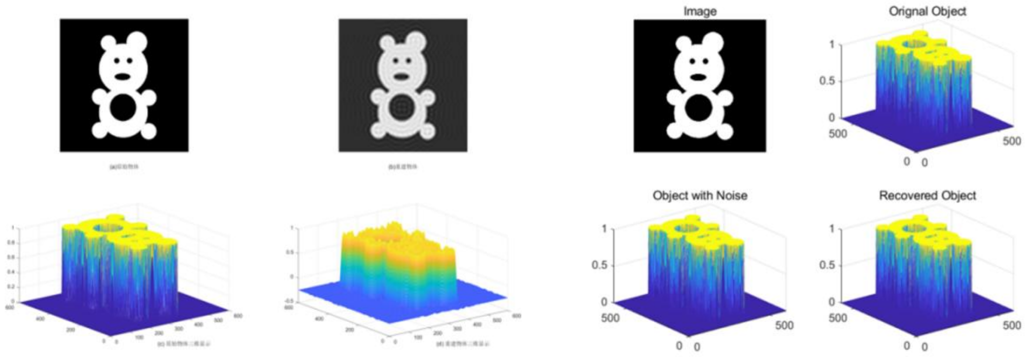

(a) Fourier method simulation (b) phase shift method simulation

Figure 16. Simulation Experiment Results

The simulation results demonstrate that while Fourier transform profilometry offers relatively faster processing speed, it is more susceptible to noise interference and requires higher-quality images. In contrast, the three-frequency four-phase method provides superior reconstruction accuracy. These findings guide our experimental preference toward employing the three-frequency four-phase approach.

3.2.2. Experimental Software.

The software component integrates various algorithms including noise removal, phase retrieval using phase-shifting method, and phase unwrapping via multi-frequency heterodyne approach, all implemented within a MATLAB-based graphical user interface (GUI). The corresponding software architecture is presented in Fig. 17, while the GUI layout is illustrated in Fig. 18.

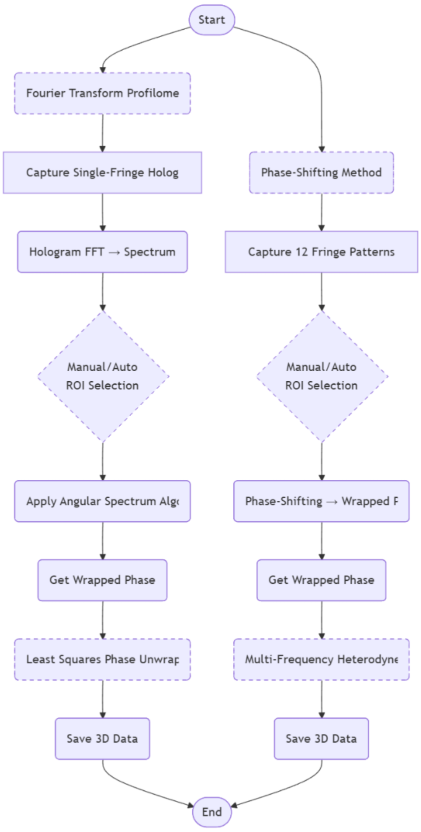

Figure 17. Software Workflow Diagram

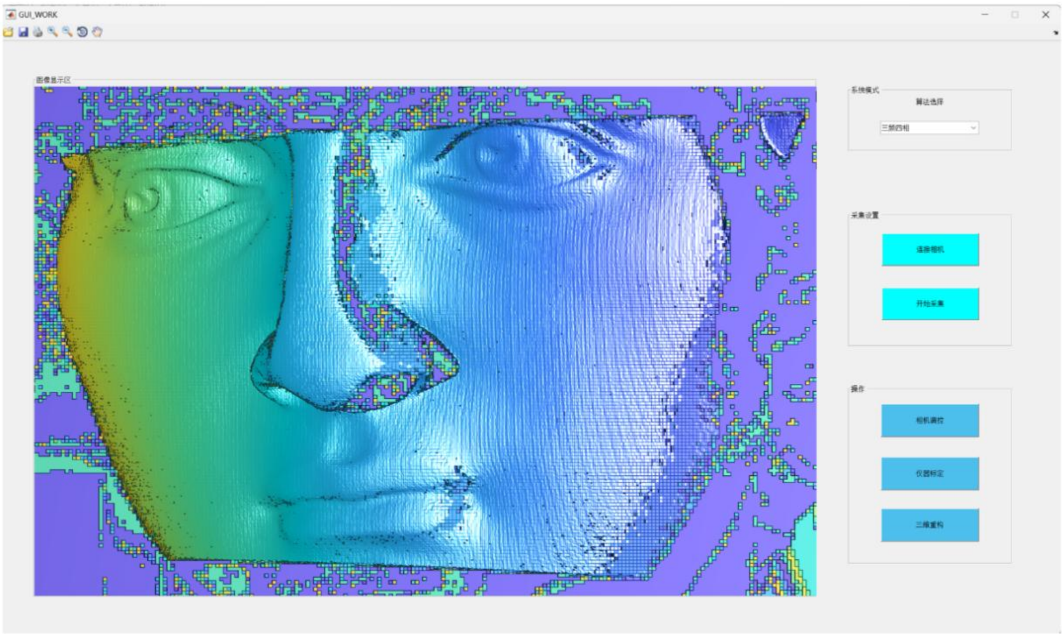

算法选择

三频四相

Figure 18. Software Interface Diagram

When starting the software, the phase retrieval method must first be selected before importing camera-captured videos or images. For Fourier transform profilometry, a Fourier transform is initially performed on the holographic image, followed by automatic or manual spectrum selection to extract either the +1st or -1st order spectrum; after spectrum extraction, the complex amplitude of the object wave is reconstructed using the angular spectrum algorithm to recover both intensity and phase, where the obtained phase is wrapped and requires least-squares phase unwrapping. For the three-frequency four-phase method, image acquisition is necessary to obtain 12 images with different phase shifts and frequencies, which are then automatically or manually cropped; after cropping, the three-frequency four-phase method is applied to recover and unwrap the wrapped phase.

4. Experiments and Data Analysis

4.1. DMD Configuration

Prior to initiating experiments, the DMD must be properly configured to ensure accurate projection of encoded sinusoidal fringes, shown in Fig.19 and 20. The DLP4500 DMD used in this study requires the following setup procedure:

(1) Structured light pattern synthesis: To maximize utilization of the DLP4500's high-speed buffer, four 8-bit images are combined into a single composite pattern. This experiment requires three such composite patterns.

(2) Initial firmware flashing: Download the official firmware, replace its default images with sinusoidal fringe patterns, save the modified firmware, and program it onto the DLP4500.

(3) Playback mode configuration: Assign each pattern to corresponding channels, establish the playback sequence, and set the exposure time (50,000 μs for this experiment).

(4) Secondary firmware flashing: Integrate the playback mode settings into the firmware and reprogram the DLP4500.

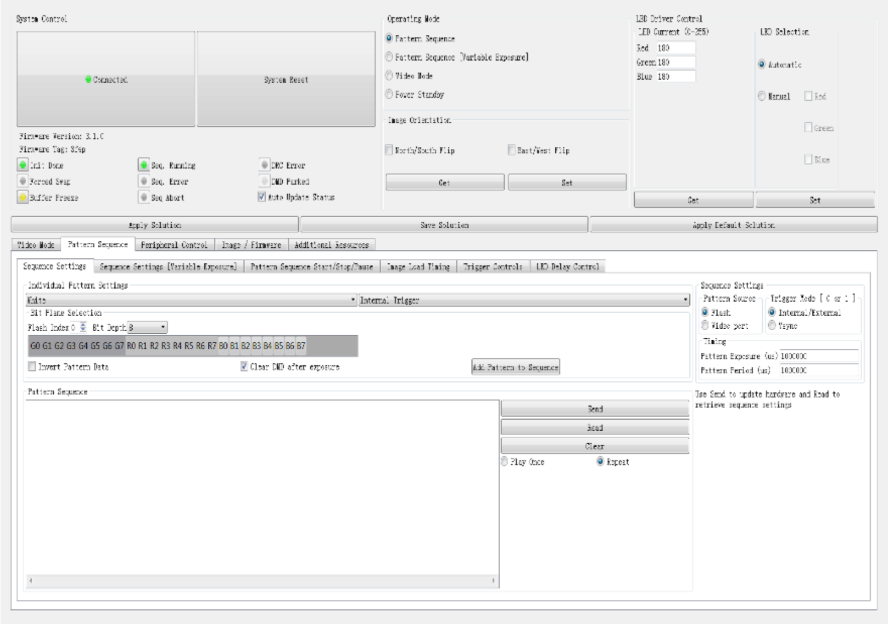

Firmware Version: 3.1.0
Firmware Tag: 5f6p

☑ Auto Update Status

● Pattern Sequence

Red 180
Green 180
Blue 180

● Automatic

White
Internal Trigger

Flash Index 0 Bit Depth 8

☐ Invert Pattern Data
☑ Clear DMD after exposure

● Flash
● Internal/External

Pattern Exposure (us) 1000000
Pattern Period (us) 1000000

Use Send to update hardware and Read to retrieve sequence settings

● Repeat

Figure 19. LightCrafter GUI Interface

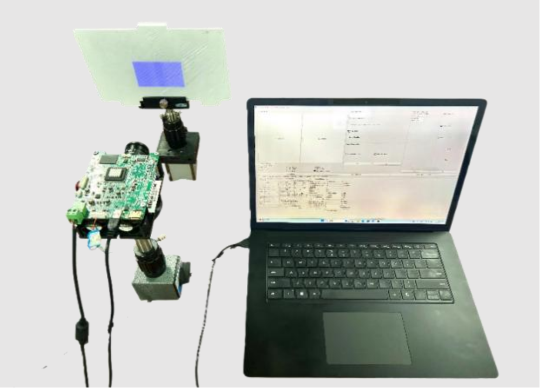

Figure 20. Practical Operation

4.2. Experimental Procedures and Precautions

The experimental setup with the complete procedure as follows:

(1) Perform system calibration to determine instrument pose and adjust optical parameters. Power off after calibration.

(2) Place the test object on the horizontal rotation stage. Power on the DMD projector to uniformly illuminate the surface with structured light.

(3) Launch the software, sequentially click "Camera On" → "Continuous Capture" to acquire distorted fringe patterns reflected from the object.

(4) Rotate the stage and repeat step (3) to capture fringe patterns at multiple angles. Power down after measurement.

(5) Analyze collected data using the software.

Critical Precautions:

(1) Maintain lens cleanliness during measurements.

(2) After calibration, all camera parameters (intrinsic/extrinsic) including pose and focal length must remain fixed.

(3) Avoid tugging or vibrating instrument cables during operation to prevent unstable projections or hardware damage.

4.3. Measurement of Facial Sculpture

Figure 21. Physical Sculpture

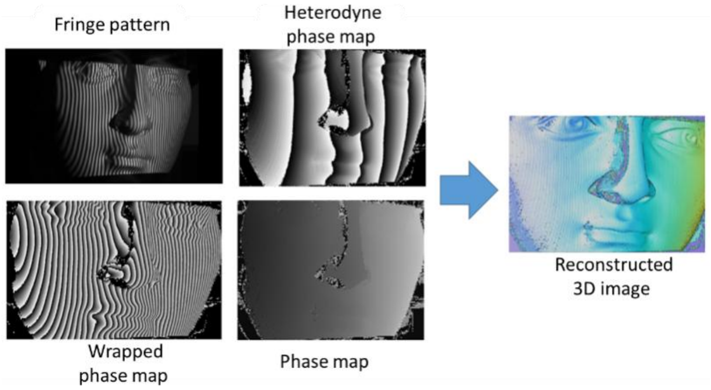

Figure 22. Phase Recovery Process Illustration

The algorithm-reconstructed process and results are presented in Fig. 22. Comparative analysis was conducted by examining key facial regions (e.g., ocular and labial areas) against the physical sculpture.

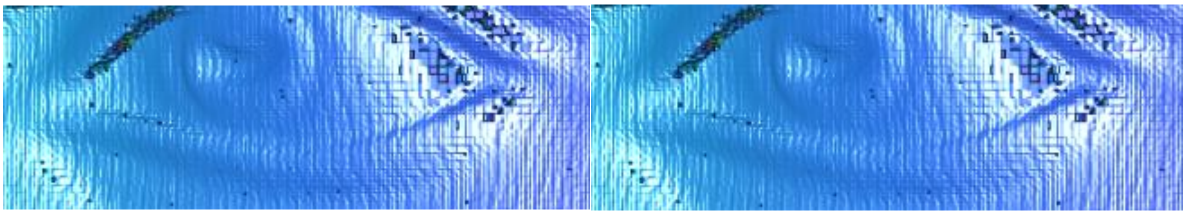

Ocular Phase Analysis

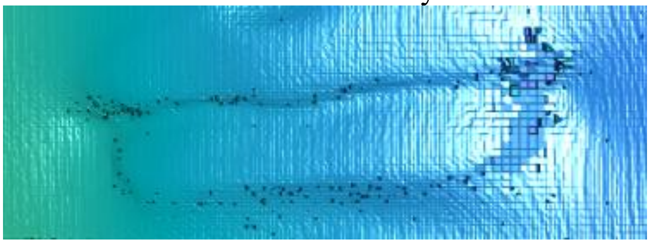

Labial Phase Analysis

Figure 23. Facial Contour Extraction

4.4. Error Analysis

(1) Errors caused by transmitted light on partial object surfaces Fringe pattern projection onto polished metals, wax-treated, transparent/semi-transparent, or smooth reflective surfaces results in contrast degradation. When the contrast loss exceeds the algorithm's recoverable threshold, it will cause significant measurement errors, and may even render the measurement system inoperable.

(2) Noise in image sensors This noise originates from random thermal motion of electrons generating weak currents, and fluctuations during the conversion between optical analog signals and digital signals.

The noise manifests in images as irregular granular brightness variations, which appear as irregular height fluctuations in the final 3D images. Our system employs the three-frequency four-phase method combined with smoothing processing to partially suppress this noise.

4.5. Limitations and Improvement Strategies

(1) The algorithm may fail to function properly when measuring translucent/reflective objects with severe contrast loss. Future improvements will adapt the algorithm to lower contrast conditions.

(2) The measurement accuracy has not yet reached the theoretical limit. Since the system's accuracy is related to fringe spacing, developing a projection system with smaller fringe spacing will achieve higher precision.

(3) The system's fast measurement speed has not been fully utilized. Future algorithm improvements to reduce latency could enable high-precision real-time 3D measurement of dynamic objects, which is significant for research in certain fields.

(4) The system has not yet been miniaturized. Future work will focus on developing a more portable and user-friendly 3D imaging system.

References

[1] WU Zhoujie, ZHANG Qican. Review on high-speed 3D shape measurement technology based on fringe projection [A]. Laser & Optoelectronics Progress, 2023, 60 (8): 01-02.

[2] HU Min. Evaluation of microstructure characteristics of surface-laminated layer by combining fringe reflection and differential spectrum segmentation [J]. Beijing Institute of Technology, 2021.

[3] WEI Yulei. Research and application of digital measurement method for surface defects of aircraft parts [C]. 2018 Military Equipment Technology Exchange Conference, 2018-09-18.

[4] Zhengyou Zhang. Flexible camera calibration by viewing a plane from unknown orientations [C]. Proceedings of the Seventh IEEE International Conference on Computer Vision, Kerkyra, Greece, 1999: 20-27 September. IEEE, 2002.

[5] LI Zhongwei. Research on structured light 3D measurement technology and system based on digital grating projection [D]. Huazhong University of Science and Technology, 2009.

[6] HUANG Tingting. Research on dynamic 3D shape measurement technology based on optical fiber interference fringe projection [J]. Tianjin University, 2022.

[7] DU Guohong. Research on 3D reconstruction system based on fringe projection structured light [J]. Yancheng Institute of Technology, 2024.